

# ODFormer: Semantic Fundus Image Segmentation Using Transformer for Optic Nerve Head Detection

Jiayi Wang, Yi-An Mao, Xiaoyu Ma, Sicen Guo, Yuting Shao, Xiao Lv, Wenting Han, Mark Christopher, Linda M. Zangwill, Yanlong Bi, and Rui Fan, *Senior Member, IEEE*

**Abstract**—Optic nerve head (ONH) detection has been an important topic in the medical community for many years. Previous approaches in this domain primarily center on the analysis, localization, and detection of fundus images. However, the non-negligible discrepancy between fundus image datasets, all exclusively generated using a single type of fundus camera, challenges the generalizability of ONH detection approaches. Furthermore, despite the numerous recent semantic segmentation methods employing convolutional neural networks (CNNs) and Transformers, there is currently a lack of benchmarks for these state-of-the-art (SoTA) networks trained specifically for ONH detection. Therefore, in this article, we first introduce ODFormer, a network based on the Swin Transformer architecture. ODFormer is designed to enhance the extraction of correlation information between features, leading to improved generalizability. In our experimental evaluations, we compare our top-performing implementation with 13 SoTA CNNs and Transformers. The results indicate that our proposed ODFormer outperforms all other approaches in ONH detection. Subsequently, we release TongjiU-DCOD dataset, the first multi-resolution mixed fundus image dataset with corresponding ONH ground-truth annotations. This dataset comprises 400 fundus images captured using two different types of fundus cameras with varying resolutions. This diversity enhances the availability of data regularity information, contributing to the improved generalizability of the model. Moreover, we establish a benchmark to thoroughly evaluate the performance for ONH detection of SoTA networks designed for semantic segmentation with extensive experiments.

This research was supported by Clinical Research Project of Tongji Hospital of Tongji University (ITJ (ZD) 2101), National Natural Science Foundation of China under Grant 82070920, the Fundamental Research Funds for the Central Universities, and Xiaomi Young Talents Program. (Corresponding author: Yanlong Bi and Rui Fan).

Jiayi Wang, Sicen Guo, and Rui Fan are with the Machine Intelligence & Autonomous Systems (MIAS) Group, the College of Electronics & Information Engineering, Shanghai Research Institute for Intelligent Autonomous Systems, the State Key Laboratory of Intelligent Autonomous Systems, and Frontiers Science Center for Intelligent Autonomous Systems, Tongji University, Shanghai 201804, China (e-mails: {1954076, guosicen, rfan}@tongji.edu.cn).

Yi-An Mao is with the Department of Bioengineering, School of Life Science, Shanghai University, 99 Shangda Avenue, Baoshan District, Shanghai, 200444 China (e-mail: maoyan@shu.edu.cn)

Xiaoyu Ma, Yuting Shao, Xiao Lv, and Wenting Han are with the Department of Ophthalmology, Tongji Hospital, School of Medicine, Tongji University, Shanghai, China (e-mails: 2031252@tongji.edu.cn; shaoyuting@tongji.edu.cn; lvxiao1212@126.com; summerh0719@163.com)

Mark Christopher and Linda M. Zangwill are with the Glaucoma Center, Department of Ophthalmology, University of California, San Diego, La Jolla (e-mails: {mac157, lzangwill}@health.ucsd.edu)

Yanlong Bi is with the Department of Ophthalmology, Tongji Hospital, School of Medicine, Tongji University, Shanghai, China; and the Tongji Eye Institute, School of Medicine, Tongji University, Shanghai, China (e-mail: bilyanlong@tongji.edu.cn)

## I. INTRODUCTION

### A. Background

Fundus images, photographs of the back of eyes, provide crucial information not only about retinal and ophthalmic conditions but also about cerebrovascular and other diseases [1]. Among the various features in a fundus image, the optic nerve head (ONH) is of particular significance [2]. The ONH typically appears as a variably sized, bright yellowish region, slightly oval in shape, with blood vessels converging towards its center [3]. It can be further divided into two distinct zones: (1) the central zone or the cup and (2) the peripheral zone or neuroretinal rim [4]. The ONH plays a crucial role in fundus image analysis, serving as a reference point for various tasks, such as fovea location estimation [5], blood vessel segmentation [2], and cup-to-disc ratio calculation [6]. Consequently, the detection of the ONH carries significant diagnostic value [7], [8]. It serves as a crucial initial step in computer-aided systems designed to assist ophthalmologists in identifying conditions such as diabetic retinopathy [9]. Moreover, ONH detection can provide additional diagnostic insights for ophthalmologists. For instance, the size of the ONH, derived from its detection, is commonly used in diagnosing glaucoma based on the cup-disc ratio [10]. Therefore, achieving precise ONH detection is of paramount importance in the field of ophthalmology, both for treatment and diagnostic purposes.

### B. Motivation

The rapid progress in deep learning technologies has led to the development of numerous semantic segmentation approaches based on neural networks, serving as powerful tools for accurate ONH detection. Compared to traditional convolutional neural networks (CNNs), the advantage of Transformers equipped with self-attention mechanisms lies in providing a more effective strategy for global context modeling [11]. Transformers have demonstrated their superiority, particularly in terms of generalizability, over CNNs across various fundamental computer vision tasks [12]. Several endeavors have been made to integrate the strengths of Transformer and CNN. For example, Polarformer [13] introduces a hybrid CNN-Transformer and polar transformation network, leveraging the Transformer's large receptive fields to incorporate global contextual information. Similarly, based on U-Net, UT-Net [14] employs a Transformer to retain learned spatial gradient information and utilize this knowledge in subsequent stages, enabling improved identification of local minor gradient changes near the boundary region. Nevertheless, despite the

excellent capabilities demonstrated by Transformers when applied to vision tasks, they still exhibit weaknesses in their performance, stemming from three factors. First, it ignores the local spatial priors within each patch when splitting images into a sequence of non-overlapping patches. Secondly, it is difficult for the Transformer to explicitly extract structural information due to the absolute positional encoding. Thirdly, the frequent application of upsampling to effectively leverage the multi-scale features generated by Transformer may result in the loss of low-resolution information, presenting a significant challenge for dense prediction tasks, such as detection and segmentation. In the dataset aspect, due to variations in fundus cameras, different fundus image datasets exhibit diverse morphological characteristics, posing a challenge for many ONH detection methods to achieve robust generalizability. For example, portable fundus cameras offer adaptability and convenience across diverse settings but may manifest a discernible variance in quality compared to professional desktop cameras. However, advanced cameras deliver high-quality images for accurate disease diagnoses but are associated with elevated costs, potentially restricting accessibility and posing challenges in specific environments due to their larger size. An additional challenge lies in the scarcity of comprehensive fundus image datasets, designed specifically to address this limitation. Existing datasets are predominantly captured using a single type of fundus camera, which hinders the facilitation of performance evaluation and generalizability of segmentation algorithms. Moreover, a notable gap exists in the absence of a dedicated benchmark for ONH detection using SoTA semantic segmentation networks. Therefore, there is a strong motivation to provide a comprehensive comparison of SoTA networks. These networks should be trained and validated across different datasets to quantify the segmentation networks' performance and generalizability.

### C. Novel Contributions

To address the above-mentioned limitations, we introduce **ONH Detection Transformer (ODFormer)**, a novel semantic segmentation network, developed specifically for ONH detection. We first present a Multi-Scale Context Aggregator (MSCA), which partitions the input image into patches while simultaneously enlarging the receptive field using a series of atrous convolutions with increasing atrous rates. Additionally, building upon the Swin Transformer [15] architecture, we design an encoder that improves the position encoding in self-attention calculations. This is achieved by integrating a relative position bias map extracted through an additional convolutional layer, obtaining more comprehensive position and order information. Regarding our ODFormer decoder, which is developed based on UperNet [16], a significant contribution lies in the Lightweight Bidirectional Feature Recalibrator (LBFR). It alleviates the loss of high-frequency spatial information resulting from both the upsampling operation and the fusion of feature maps within the pyramid structure. Moreover, we publish a large-scale, comprehensive fundus image dataset, referred to as **Tongji University Dual-Resolution ONH Detection (TongjiU-DRD)** dataset. For each participant, fundus images were captured using

two distinct cameras, and the semantic segmentation ground-truths for these images were manually annotated. We establish an ONH detection benchmark using our published TongjiU-DRD dataset, in conjunction with two publicly available datasets: DRIONS-DB [17] and DRISHTI-GS1 [18]. This benchmark facilitates qualitative and quantitative comparisons of state-of-the-art (SoTA) CNNs for ONH detection. Extensive experimental results demonstrate that (1) the effectiveness of our designed modules within ODFormer, (2) its superior performance and generalizability across various datasets, and (3) the suitability of our curated dataset for training and evaluating ONH detection networks.

In summary, the contributions of this article are as follows:

- A novel network, referred to as ODFormer, with technical contributions in three aspects: (1) context aggregation using atrous convolutions, (2) a convolutional position bias map for self-attention calculation, and (3) feature recalibration through spatial separable convolutions. It outperforms SoTA CNNs and Transformers for ONH detection;
- A dataset for ONH detection captured using two different cameras;
- A benchmark of SoTA semantic segmentation CNNs and Transformers trained on the three aforementioned datasets for ONH detection.

### D. Paper Structure

The remainder of this article is structured as follows: Sect. II reviews the SoTA CNNs-based and Transformer-based semantic segmentation networks. Sect. III introduces our proposed ODFormer. Sect. IV details our proposed TongjiU-DRD dataset. Sect. V presents the experimental results and compares our framework with other SoTA networks. Finally, we conclude this article in the last section.

## II. LITERATURE REVIEW

### A. Convolutional Neural Networks for Semantic Segmentation

Fully Convolutional Network (FCN) [19] pioneers the era of end-to-end segmentation, which is now the most advanced and robust framework for scenario analysis. In traditional CNNs, several fully connected layers will be connected after the final convolutional layer. It converts a feature map into a feature vector with a fixed length. FCN, on the other hand, can accept input images of any size and upsample the feature map of the final layer using a deconvolution layer. Therefore, the output eventually recovers to the original image size and produces a prediction for each pixel while preserving the spatial information in the original input image. However, the ability of FCN-based models to utilize global scene category clues is limited. Pyramid Scene Parsing Network (PSPNet) [20] performs spatial pooling at several grid scales and demonstrates outstanding performance on several semantic segmentation benchmarks. It fuses the global pyramid pooling structure for pixel-level feature expansion with the traditional extended FCN [21] architectural idea for pixel prediction. PSPNet does not add many parameters over the FCN network

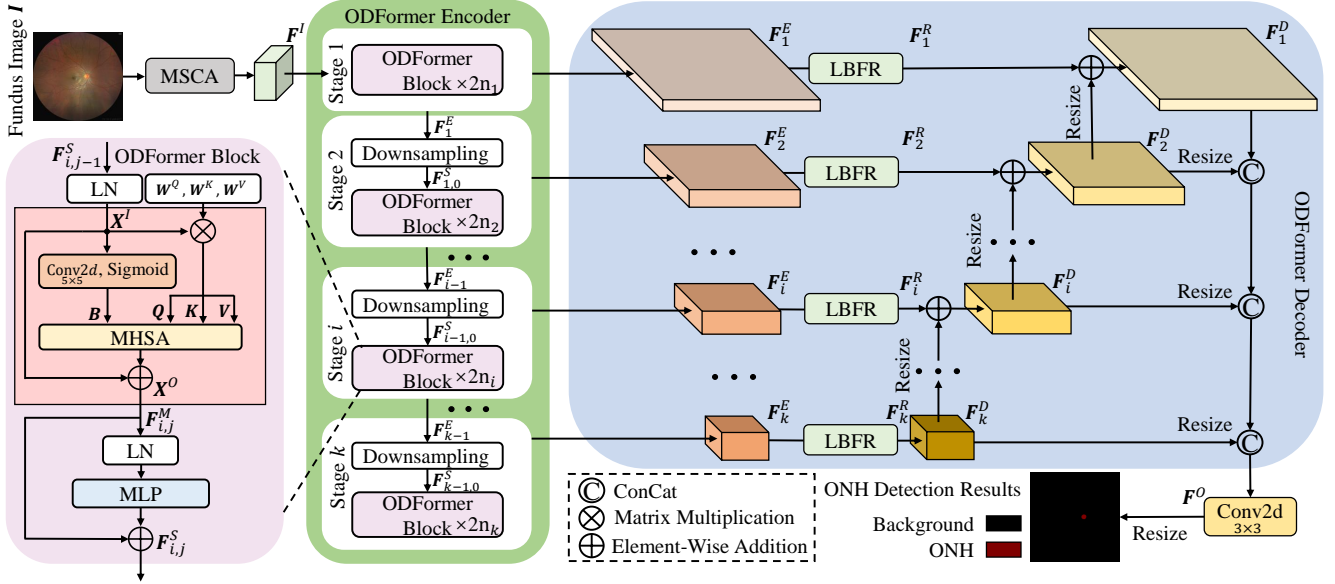


Fig. 1: An overview of our proposed ODFormer framework.

architecture in terms of computational cost. Feature Pyramid Network (FPN) [22] is a general-purpose feature extractor that takes advantage of multi-level feature representations in a pyramidal, natural hierarchy. With only a small additional computational cost, it leverages a top-down design with lateral connections to combine high-level semantic information with medium and low levels. Moreover, Unified Perceptual Parsing Network (UPerNet) [16] highly integrates architecture and Pyramid Pooling Module (PPM) from PSPNet [20], which solves the problem of relatively small empirical receptive field of deep CNN.

In contrast to carrying out pooling operations at various grid scales like PSPNet, DeepLabv3 [23] employs several parallel atrous convolutions (ASPP) with different rates to gather contextual data of various scales. The most recent feature map encodes rich semantic information, but details of object boundaries are missing due to pooling and convolutions with striding operations in the network backbone. DeepLabv3+ [24] adds a concise yet efficient decoder module to DeepLabv3 to improve segmentation results, particularly along label boundaries. ASPP [23] and PPM [20] employ predefined convolution with different dilation rates and multi-scale pooling operations. Both methods are sensitive not only to the size of the input images but also to the scale differences between images in the training and inference phases. The internal scale variation of the input images with arbitrary scales and sizes cannot be obtained by fixed weights, predefined dilation rates and pooling grids.

The self-attention module affects an individual element by aggregating features from a set of elements. The aggregation weights are typically based on embedded feature similarities between the elements. They are effective at capturing contexts and long-range dependencies. With the frequent use of attention mechanism in neural networks, Non-local neural network

[25] obtains the attention mask by calculating the correlation matrix between each spatial point in the feature map. However, the prohibitive computational cost and vast GPU memory occupation of Non-local neural network hinder its usage in many real applications. Asymmetric Non-local Neural Network (ANN) [26] samples only a few representative points from feature maps, which can dramatically improve the efficiency and decrease the memory consumption of non-local neural blocks without sacrificing the performance. The subsequent Global Context Network (GCNet) [27] simplified the non-local block by calculating a global attention map and sharing it for all locations, which greatly reduced the amount of calculation. Dual Attention Network (DANet) [28] encodes global context with well well-designed self-attention mechanism and incorporates both spatial and channel attention. Although DANet [28] uses adaptive weights to calculate pair-wise similarity or learn pixel-wise attention maps, it overlooks the significance of global guidance from the global information extractor. In contrast, APCNet [61] takes global-guided local affinity into account to estimate the degree of subregion contribution from local and global representations and exploits multi-scale representation with a feature pyramid. Dynamic Multi-scale Network (DMNet) [29] learns variable-scale features with dynamic multi-scale filters which can adaptively select important areas to enable the model to better extract contextual information. It is more adaptable and flexible because each branch can capture a unique scale feature related to the input image.

### B. Transformers for Semantic Segmentation

Transformers [30] rely on self-attention mechanisms and capture long-range dependencies among tokens in a sentence. In addition, transformers are well suited for parallelization and facilitating training on large datasets. The success of transformers in NLP has inspired several methods in com-

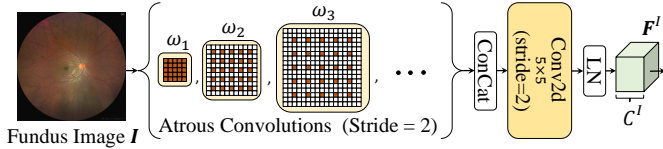


Fig. 2: The architecture of multi-scale context aggregator.

puter vision combining CNNs with self-attention mechanisms to address semantic segmentation problems [31]. Based on Transformer, Object-Contextual Representation (OCR) [32] uses the representation of the corresponding object class to characterize a pixel, which strengthens the pixel representation. Moreover, Swin Transformer [15] uses a variant of ViT [33], and proposes a hierarchical Transformer whose representation is computed with a shifted window. This hierarchical architecture has the flexibility to model at multiple scales and has different linear computational complexity with regard to image size.

### III. METHODOLOGY

The architecture of our developed ODFormer is illustrated in Fig. 1. It consists of three main components:

- A multi-scale context aggregator for feature initialization.
- An ODFormer encoder for the extraction of hierarchical feature maps from RGB images.
- An ODFormer decoder that recursively refines and fuses the multi-scale feature maps to generate the final semantic predictions.

#### A. Multi-Scale Context Aggregator

To transform the given fundus image  $\mathbf{I} \in \mathbb{R}^{H \times W \times 3}$  into a sequence of patches suitable for processing with the Transformer, with  $H$  and  $W$  representing the height and width of the image, respectively, the conventional ViT model directly splits the fundus image into non-overlapping patches using linear projection [33]. Nevertheless, the ViT architecture poses a significant challenge concerning the absence of long-range dependencies, primarily due to its limited receptive fields. This limitation holds paramount importance in semantic segmentation tasks. To overcome this limitation, we design an MSCA, which first utilizes a series of  $m$  atrous convolutions  $\omega_d$  ( $d \in [1, m] \cap \mathbb{Z}$  representing the atrous rate) to extract multi-scale feature maps, which are then aggregated for feature initialization. As the network's depth increases, the atrous rates progressively become larger, leading to an expanded receptive field. This process can be formulated as follows:

$$\mathbf{F}^I = \text{LN} \left( \text{Conv2d}_{5 \times 5} \left( \text{ConCat}_{d \in [1, m]} (\omega_d(\mathbf{I})) \right) \right) \in \mathbb{R}^{\frac{H}{4} \times \frac{W}{4} \times C^I}, \quad (1)$$

where Conv2d denotes a 2D convolution layer, ConCat( $\cdot$ ) represents a concatenation operation performed in the channel dimension,  $\mathbf{F}^I$  denotes the initialized feature maps, which are subsequently fed into our ODFormer encoder, and  $C^I$  represents the channel number of  $\mathbf{F}^I$ . Sect. V-B details the

experiments conducted to demonstrate the effectiveness of our proposed MSCA.

#### B. ODFormer Encoder

Our ODFormer encoder is designed based on Swin Transformer to generate hierarchical feature maps. Our ODFormer encoder contains  $k$  stages, in each stage,  $2n_i$  ODFormer blocks are stacked sequentially for feature transformation. The input feature maps  $\mathbf{F}_{i,j-1}^S$  are first processed through a novel multi-head self-attention (MHSA) block that incorporates relative position bias to produce the intermediate feature maps  $\mathbf{F}_{i,j}^M$ , which are subsequently processed by a multi-layer perceptron (MLP) to generate the encoded feature maps  $\mathbf{F}_{i,j}^S$ , where  $\mathbf{F}_{i,j-1}^S, \mathbf{F}_{i,j}^M, \mathbf{F}_{i,j}^S \in \mathbb{R}^{\frac{H}{2^{i+1}} \times \frac{W}{2^{i+1}} \times (2^{i-1}C^I)}$  ( $i \in [1, k] \cap \mathbb{Z}, j \in [1, 2n_i] \cap \mathbb{Z}$ ).

ViT performs self-attention calculations on the input features in a parallel and uniform manner, which results in the neglect of order and position information within the sequence [33]. In contrast, the Swin Transformer incorporates absolute positional encoding to account for the order of tokens [15]. However, this approach introduces unique positional encoding for each patch, compromising invariance and neglecting local relationships and structural information within patches. To address this issue, we introduce an additional convolutional layer to extract a relative position bias map and incorporate a residual connection to ensure stable model training. When performing self-attention calculations, let  $\mathbf{X}^I = \text{LN}(\mathbf{F}_{i,j-1}^S) \in \mathbb{R}^{M^2 \times d}$  and  $\mathbf{X}^O \in \mathbb{R}^{M^2 \times d}$  be the input and output matrices, respectively, where LN( $\cdot$ ) denotes layer normalization,  $M$  denotes the side length of each patch, and  $d$  represents the query/key dimension. We first construct the relative position bias map for each head, as follows:

$$\mathbf{B}_r = \text{Sigmoid}(\text{Conv2d}_{3 \times 3}(\mathbf{X}^I)) \in \mathbb{R}^{M^2 \times M^2}, \quad r \in [1, N_h], \quad (2)$$

where  $N_h$  denotes the number of heads. Subsequently, the query matrix  $\mathbf{Q} = \mathbf{X}^I \mathbf{W}^Q \in \mathbb{R}^{M^2 \times d}$ , key matrix  $\mathbf{K} = \mathbf{X}^I \mathbf{W}^K \in \mathbb{R}^{M^2 \times d}$ , and value matrix  $\mathbf{V} = \mathbf{X}^I \mathbf{W}^V \in \mathbb{R}^{M^2 \times d}$  are learned for each head, where  $\mathbf{W}^{Q,K,V} \in \mathbb{R}^{d \times d}$  are linear projection matrices. Then  $\mathbf{Q}, \mathbf{K}, \mathbf{V}$  are evenly divided into  $N_h$  equal parts along the dimension direction, and each part is  $\mathbf{Q}_r, \mathbf{K}_r, \mathbf{V}_r \in \mathbb{R}^{M^2 \times \frac{d}{N_h}}$ . A multi-head self-attention is then performed as follows:

$$\mathbf{H}_r = \text{Softmax} \left( \frac{\mathbf{Q}_r \mathbf{K}_r^\top}{\sqrt{\frac{d}{N_h}}} \right) \times \mathbf{V}_r + \mathbf{B}_r. \quad (3)$$

$\mathbf{X}^O$  can therefore be obtained through:

$$\mathbf{X}^O = \text{ConCat}_{r \in [1, N_h]} (\mathbf{H}_r) + \mathbf{X}^I. \quad (4)$$

The output feature maps  $\mathbf{F}_{i,j}^S$  can then be yielded through:

$$\mathbf{F}_{i,j}^S = \text{MLP}(\text{LN}(\mathbf{F}_{i,j}^M)) + \mathbf{F}_{i,j}^M. \quad (5)$$

To produce hierarchical features, our ODFormer block reduces the spatial resolution of the input features through downsampling:

$$\mathbf{F}_{i,0}^S = \text{LN}(\text{Conv2d}_{3 \times 3}(\mathbf{F}_{i-1, 2n_{i-1}}^S)), \quad (i \neq 1). \quad (6)$$

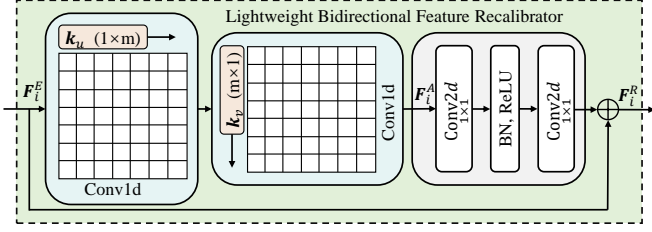


Fig. 3: The architecture of lightweight bidirectional feature recalibration.

The hierarchical encoder feature maps  $\mathcal{F}^E = \{\mathbf{F}_1^E, \dots, \mathbf{F}_k^E\}$ , where  $\mathbf{F}_i^E = \mathbf{F}_{i,2n_i}^S$ , can therefore be extracted.

### C. ODFormer Decoder

We design our ODFormer decoder based on UperNet [16] to recursively recalibrate and fuse the hierarchical feature maps extracted by our ODFormer encoder. However, the use of simplistic upsampling operations, such as bilinear interpolation, can lead to the loss of local information, resulting in unsatisfactory boundary details in semantic segmentation. To overcome this limitation, we aim to incorporate more relevant local information into the features before performing upsampling. To achieve this, we design an LBFR (see Fig. 3) to capture additional local information while simultaneously reducing computational complexity and the number of network parameters. This approach allows us to enhance the representation of local details in the fundus segmentation process.

Our LBFR first extracts an attention map  $\mathbf{F}_i^A \in \mathbb{R}^{\frac{H}{2^{i+1}} \times \frac{W}{2^{i+1}} \times C^D}$  from the encoder feature maps  $\mathbf{F}_i^E$ . In this process, the conventional 2D convolution with a large kernel size is replaced with two 1D spatial separable convolutions, as follows:

$$\mathbf{F}_i^A = \mathbf{k}_v \circledast (\mathbf{k}_u \circledast \mathbf{F}_i^E), \quad (7)$$

where  $\circledast$  denotes the convolution operation, and  $\mathbf{k}_u$  and  $\mathbf{k}_v$  represent 1D convolutions that operate in the horizontal and vertical directions, respectively. The performance comparison of different convolutional strategies that possess receptive fields of the same size are presented in Sect. V-B. The original encoder feature maps  $\mathbf{F}_i^E$  are then recalibrated and fused through:

$$\mathbf{F}_i^R = \text{Conv}_{1 \times 1}^2d \left( \text{ReLU} \left( \text{BN} \left( \text{Conv}_{1 \times 1}^2d \left( \mathbf{F}_i^A \right) \right) \right) \right) + \mathbf{F}_i^E. \quad (8)$$

Our ODFormer decoder recursively generates a collection of  $k$  decoder feature maps  $\mathcal{F}^D = \{\mathbf{F}_k^D, \dots, \mathbf{F}_1^D\}$ , where

$$\mathbf{F}_i^D = \mathbf{F}_i^R + \text{Resize}(\mathbf{F}_{i+1}^D), \quad (i \in [1, k] \cap \mathbb{Z}), \quad (9)$$

where  $\text{Resize}(\cdot)$  denotes the resizing operation via bilinear interpolation. The output feature maps from the ODFormer decoder are obtained through:

$$\mathbf{F}^O = \text{Conv}_{3 \times 3}^2d \left( \text{ConCat}_{i \in [1, k]} \left( \text{Resize}(\mathbf{F}_i^D) \right) \right) \in \mathbb{R}^{\frac{H}{4} \times \frac{W}{4} \times K}, \quad (10)$$

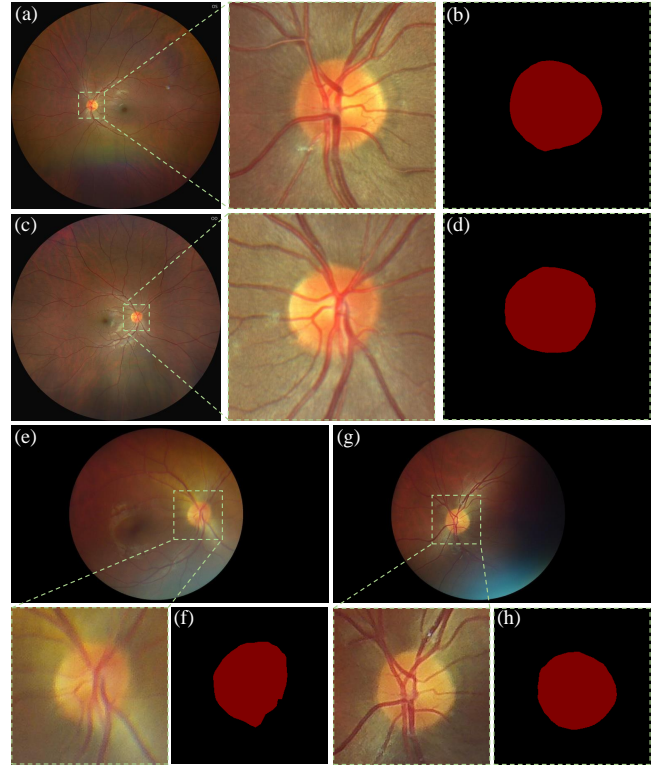


Fig. 4: Examples of fundus images from a single participant captured using two different cameras. (a)-(d) are the fundus images captured using a Zeiss CLARUS 500 fundus camera and their ground-truth annotations, (e)-(h) are the fundus images captured using an NES-1000P handheld mydriasis-free portable fundus camera and their ground-truth annotations.

where  $K$  represents the total number of classes. Finally,  $\mathbf{F}^O$  is passed through a bilinear layer to match the size of the input fundus image  $\mathbf{I}$  for segmentation.

## IV. DATASETS

We first summarize the existing datasets created for ONH detection in Sect. IV-A. Then we present a detailed description of our published TongjiU-DCOD dataset in Sect. IV-B.

### A. Existing Datasets

- DRIONS-DB [17] contains 110 pairs of fundus images (resolution:  $600 \times 400$  pixels), each with two manually-labeled ground-truth annotations. 90 pairs are used for model training, while the remaining 20 pairs are used for model validation. Within these images, 50 instances exhibit various defects, including illumination artifacts, rim blurredness, and papillary atrophy. These defects could potentially pose challenges to the accurate segmentation of fundus images [3].
- DRISHTI-GS1 [18] contains 101 pairs of high-resolution fundus images (resolution:  $2,470 \times 1,760$  pixels) including samples from both healthy and glaucomatous eyes. 81 pairs of images are used for model training, while the remaining 20 pairs of images are used for model validation. For each image in the DRISHTI-GS1 dataset,

ground-truth annotations are collected for both ONH and cup regions. These annotations are obtained through the input of four different human experts with varying levels of clinical experience. The average boundaries for both the ONH and cup regions are derived from the manually marked boundaries provided by these experts.

Nonetheless, it is important to note that both these datasets were generated exclusively using a single type of fundus camera. Consequently, semantic segmentation models trained solely on either of these datasets may demonstrate limited generalizability, primarily because of the limited diversity in the data sources. Therefore, one of our primary objectives is to create a diverse fundus image dataset, comprising images captured using various types of fundus cameras. This dataset will facilitate the evaluation of the generalizability of ONH detection networks across different imaging devices.

### B. TongjiU-DCOD Dataset

1) *Data Collection:* The data collection process involves 147 participants, ranging in age from 18 to 30 years, with an even distribution of males and females. All images were collected with the explicit consent of the participants. 53 participants contributed data from both eyes, while 94 participants provided data from a single eye. The fundus image of each eye was captured by two experts using different cameras, resulting in two fundus images per eye.

Considering that early indications of disease are often subtle and challenging to discern through direct observation or low-resolution fundus imaging, we first employed a Zeiss CLARUS 500 fundus camera to acquire high-resolution images (resolution:  $3,912 \times 3,912$  pixels), with the macula at the center, providing a field of view of approximately  $133^\circ$ . The Zeiss CLARUS 500 fundus camera is renowned for its true color, high-definition capabilities, and ultra-wide-angle field of view, enabling the capture of high-resolution fundus images with exceptional clarity, achieving resolutions as fine as 7 microns, ranging from the macula to the far periphery.

Moreover, fundus images (resolution:  $1,920 \times 1,088$  pixels), with a field of view of approximately  $40^\circ$ , were also captured using an NES-1000P handheld mydriasis-free portable fundus camera provided by Shanghai New Eyes Medical Co., Ltd. Its lightweight and portable design makes it an ideal tool for clinicians who need the flexibility to perform remote examinations or lack access to a desktop fundus camera.

2) *Ground Truth Annotation:* Our TongjiU-DCOD dataset was developed in collaboration with three ophthalmologists who were responsible for participant selection, image selection, and diagnosis assignment. Furthermore, two experts independently provided manual ONH ground-truth annotations, which were subsequently reviewed and refined by a senior expert. Fig. 4 illustrates an example of four fundus images obtained from two eyes belonging to the same participant, along with their respective ground-truth annotations.

3) *Dataset Preparation:* The data collection process described above yielded a total of 400 pairs of fundus images, among which 360 pairs are used for model training, while the remaining 40 pairs are used for model validation. To avoid potential bias introduced by the similarity of fundus

images taken from the same participant, we determined the training and validation sets based on individual participants. This strategy guarantees that fundus images from a given participant do not appear in both the training and validation sets simultaneously.

## V. EXPERIMENTAL RESULTS

In this section, we investigate the effectiveness of ODFormer architecture by conducting segmentation experiments on three datasets. We first ablate the important elements of ODFormer, and then compare the proposed ODFormer with previous SoTA models on the above datasets.

### A. Experimental Setup

We utilize two publicly available fundus image datasets DRISHTI-GS1, DRIONS-DB, and our TongjiU-DCOD dataset in our experiments to compare the performance of different methodologies. We compare the performance of fourteen semantic segmentation models including our proposed network. These methods include different architectures based on CNN and Transformer. All experiments are conducted with NVIDIA RTX 3090 GPU. Additionally, we employ various data augmentation techniques, such as cropping, flipping, and optical warping, to enhance the models' robustness. Moreover, we resize the images within a specific range while maintaining the aspect ratio constant. For fair comparisons, we adopt the same training and augmentation strategy in all experiments. All the networks undergo training for the same number of iterations and then select the best model according to the performance of the validation set. We use the Stochastic Gradient Descent (SGD) optimizer uniformly to optimize the models. Three common evaluation metrics are employed to quantify the model performance: accuracy (Acc), F-score (Fsc), and the Intersection over Union (IoU).

Fig. 5 shows the visualization of ONH detection results with different training architectures trained on TongjiU-DCOD. Next, we conduct ablation studies in Sect. V-B to demonstrate the effectiveness of our novelities. Then, an ONH detection benchmark that provides a detailed performance comparison between the 13 SoTA networks and our ODFormer on the three datasets is presented in Sect. V-C.

### B. Ablation Study

We adopt Swin Transformer as the baseline network because it outperforms all other SoTA networks. To prove the effectiveness of the branch structure in MSCA, we test MSCA with  $m \in [1, 8]$  atrous convolutions. As shown in Table I, as the number of atrous convolutions increases, the detection performance gradually improves and finally stabilizes when  $m = 3$ . Therefore, in the following experiments, we employ MSCA with three atrous convolutions. The results demonstrate that our MSCA exhibits superior performance when integrated with the Swin Transformer, achieving improvements of 0.39%-7.51% in terms of IoU and 1.15%-21.14% in terms of Fsc.

Since the LBFR is designed specifically to decrease network parameters while maintaining an unchanged receptive field size, our investigation focuses on various convolutional

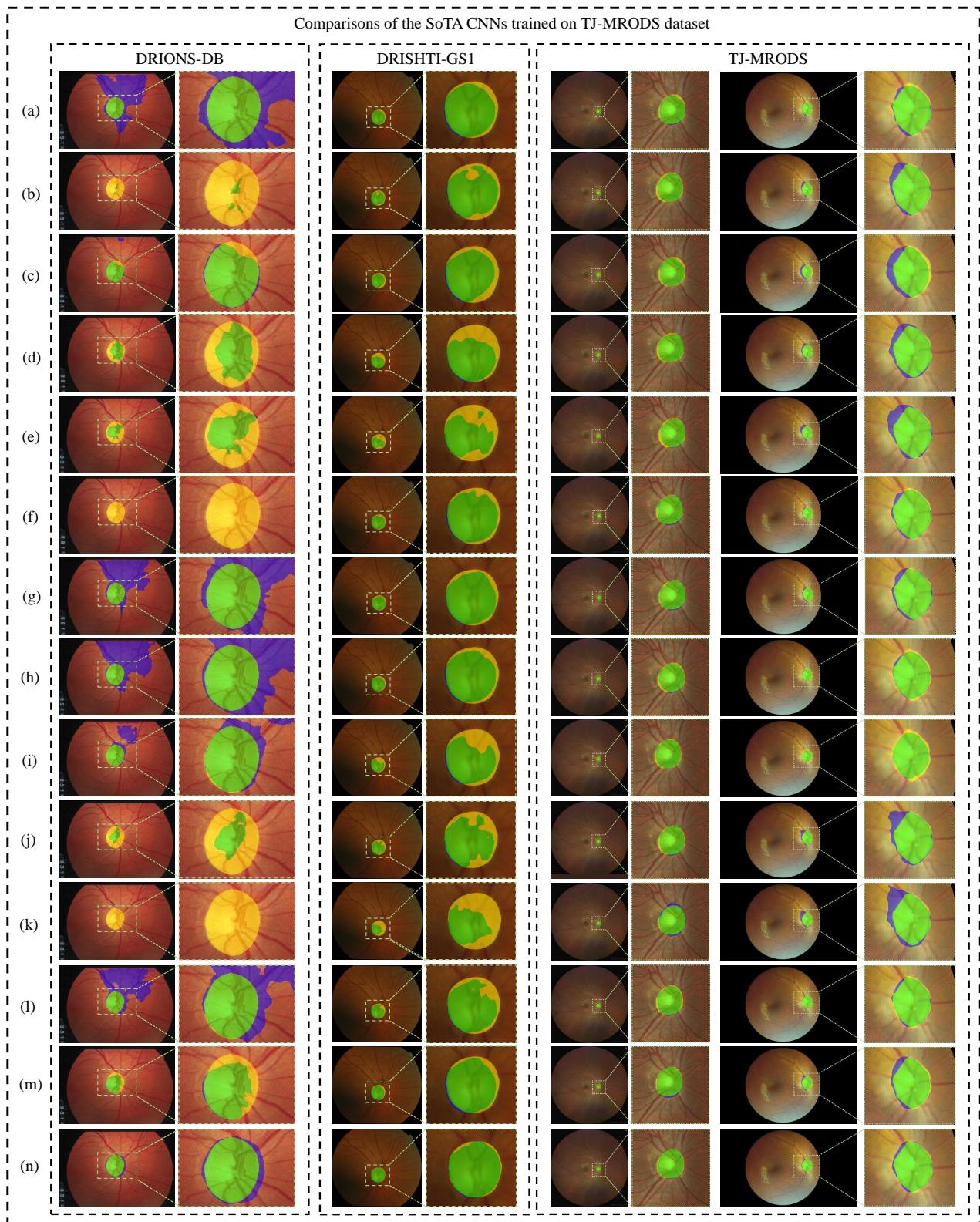


Fig. 5: Examples of ONH detection results trained on TongjiU-DCOD dataset: (a) FCN [19]; (b) PSPNet [20]; (c) FPN [22]; (d) UperNet [16]; (e) Deeplab v3 [34]; (f) NonLocal [25]; (g) ANN [26]; (h) GCNet [27]; (i) DANet [28]; (j) APCNet [35]; (k) DMNet [29]; (l) OCRNet [32]; (m) Swin Transformer [15]; (n) ODFormer(ours).

TABLE I: the segmentation results of MSCA with different atrous convolutions, the best results of testing on these three datasets are bolded.

	Method	IoU (%)	Acc (%)	Fsc (%)
TongjiU-DCOD	Swin-T	87.27	93.20	90.54
	+ MSCA ( $m = 1$ )	87.27	93.20	90.54
	+ MSCA ( $m = 2$ )	87.53	93.35	95.45
	+ MSCA ( $m = 3$ )	87.81	93.51	94.06
	+ MSCA ( $m = 4$ )	88.05	93.64	92.53
	+ MSCA ( $m = 5$ )	88.09	93.67	91.42
	+ MSCA ( $m = 6$ )	88.21	93.74	93.06
	+ MSCA ( $m = 7$ )	88.27	93.77	92.85
	+ MSCA ( $m = 8$ )	88.44	93.87	93.19
DRIONS-DB	Swin-T	91.12	95.36	96.83
	+ MSCA ( $m = 1$ )	91.14	95.36	97.39
	+ MSCA ( $m = 2$ )	91.14	95.36	97.39
	+ MSCA ( $m = 3$ )	91.37	95.49	97.98
	+ MSCA ( $m = 4$ )	91.43	95.52	96.83
	+ MSCA ( $m = 5$ )	91.45	95.54	96.58
	+ MSCA ( $m = 6$ )	91.26	95.43	97.93
	+ MSCA ( $m = 7$ )	91.51	95.57	97.69
	+ MSCA ( $m = 8$ )	91.30	95.45	97.96
DRISHTI-GS1	Swin-T	86.28	54.81	77.15
	+ MSCA ( $m = 1$ )	91.99	95.83	97.32
	+ MSCA ( $m = 2$ )	92.03	95.85	97.72
	+ MSCA ( $m = 3$ )	92.70	96.21	98.29
	+ MSCA ( $m = 4$ )	93.08	96.41	92.45
	+ MSCA ( $m = 5$ )	93.08	96.42	95.35
	+ MSCA ( $m = 6$ )	93.13	96.44	96.97
	+ MSCA ( $m = 7$ )	93.60	96.96	96.69
	+ MSCA ( $m = 8$ )	93.79	96.79	97.13

strategies that possess receptive fields of the same size as the LBFR. As shown in Table II, Strategy (A) involves replacing two 1D spatial separable convolutions in LBFR with three  $3 \times 3$  convolutions, while Strategy (B) replaces them with one  $3 \times 3$  convolution followed by one  $5 \times 5$  convolution, Strategy (C) replaces them with one  $7 \times 7$  convolution. The results indicate that our LBFR exhibits superior detection performance and generalizability compared to other strategies. It achieves an improvement of 0.77% to 1.63% in terms of IoU, as well as an enhancement in IoU on external datasets ranging from 0.02% to 21.97%. The observed improvement underscores the efficacy of our LBFR approach, which additionally boasts minimal network parameters.

Furthermore, we evaluate the individual effectiveness of MSCA and LBFR, as well as their compatibility. The networks are trained on three datasets. The results shown in Table III indicate that (1) MSCA achieves an improvement of up to 0.36% in IoU on the same dataset, and an IoU increase on external datasets of up to 6.15%, (2) LBFR results in a maximum IoU improvement of 0.77% compared to the baseline setup, as well as an IoU improvement on external datasets of up to 21.97%, and (3) the combined utilization

TABLE II: Ablation study of our proposed LBFR on three datasets, then the best results of testing on these three datasets are bolded.

	Method	TongjiU-DCOD	DRIONS-DB IoU (%)	DRISHTI-GS1
TongjiU-DCOD	Swin-T	87.45	68.27	86.01
	+ strategy (A)	86.75	<b>73.48</b>	<b>90.62</b>
	+ strategy (B)	87.61	68.54	86.92
	+ strategy (C)	86.60	72.61	88.29
	+ LBFR	<b>88.22</b>	70.57	86.03
DRIONS-DB	Swin-T	53.51	90.07	83.76
	+ strategy (A)	34.57	90.83	86.85
	+ strategy (B)	54.66	90.13	86.91
	+ strategy (C)	59.70	90.35	79.98
	+ LBFR	<b>75.48</b>	<b>90.49</b>	<b>86.21</b>
DRISHTI-GS1	Swin-T	40.27	83.46	92.05
	+ strategy (A)	51.69	80.97	92.86
	+ strategy (B)	47.87	83.21	93.28
	+ strategy (C)	50.24	<b>83.55</b>	92.88
	+ LBFR	<b>59.92</b>	80.79	<b>93.68</b>

TABLE III: Ablation study demonstrating the effectiveness of our proposed MSCA and LBFR, the best results of testing on these three datasets are bolded.

	MSCA	LBFR	TongjiU-DCOD	DRIONS-DB IoU (%)	DRISHTI-GS1
TongjiU-DCOD	×	×	87.45	68.27	86.01
	✓	×	87.81	<b>74.27</b>	87.37
	×	✓	88.22	70.57	86.03
	✓	✓	<b>88.35</b>	74.18	<b>88.39</b>
DRIONS-DB	×	×	53.51	90.47	83.76
	✓	×	59.66	<b>91.37</b>	86.05
	×	✓	<b>75.48</b>	90.49	86.21
	✓	✓	68.52	90.53	<b>86.43</b>
DRISHTI-GS1	×	×	40.27	83.46	92.05
	✓	×	45.05	81.69	92.70
	×	✓	50.78	81.89	92.41
	✓	✓	<b>63.69</b>	<b>83.93</b>	<b>93.91</b>

of MSCA and LBFR modules yields better performance than using these modules solely.

### C. ONH Detection Benchmark

This subsection presents an ONH detection benchmark with quantitative and qualitative comparisons among 13 SoTA networks and our ODFormer trained on the three aforementioned datasets. Fig. 5 presents some examples of qualitative results, from which it can be found that our ODFormer presents more accurate and robust results than all other SoTA networks across TongjiU-DCOD dataset with the same input. Additionally, the quantitative comparisons are given in Table IV. It can be clearly observed that the superior performance and enhanced generalizability of our ODFormer over all the other networks in ONH detection underscore the effectiveness

TABLE IV: The ONH detection benchmark was conducted with twelve SoTA CNNs, two Transformer-based networks, and our ODFormer on three datasets. The best results are shown in bold type.

	Method	TongjiU-DCOD			DRIONS-DB			DRISHTI-GS1		
		IoU (%)	Fsc (%)	Acc (%)	IoU (%)	Fsc(%)	Acc (%)	IoU (%)	Fsc (%)	Acc (%)
TongjiU-DCOD	FCN [19]	86.16	92.56	91.91	8.83	16.23	<b>99.69</b>	33.26	49.92	92.87
	PSPNet [20]	86.07	92.51	90.06	31.76	48.21	33.09	66.29	79.72	67.61
	FPNNet [22]	84.11	91.37	89.93	28.92	44.86	83.30	79.58	88.63	90.64
	UperNet [16]	85.67	92.28	94.26	38.82	55.93	40.42	57.45	72.97	59.53
	DeepLab v3 [34]	86.65	92.85	92.33	40.35	57.50	42.56	67.38	80.51	70.63
	NonLocal [25]	87.84	93.52	93.67	29.02	44.99	29.97	62.64	77.03	63.76
	ANN [26]	86.88	92.98	94.33	12.59	22.36	98.94	75.02	85.73	92.27
	GCNet [27]	87.67	93.43	92.03	9.33	17.07	98.68	79.82	88.78	87.92
	DANet [28]	87.41	93.28	90.28	10.84	19.56	95.82	81.43	89.77	84.40
	APCNet [35]	85.77	92.34	91.60	37.12	54.15	38.92	69.73	82.16	72.20
	DMNet [29]	80.34	89.10	90.09	15.58	26.96	15.66	35.73	52.65	36.16
	OCRNet [32]	87.18	93.15	91.40	20.74	34.35	86.69	80.09	89.44	82.93
	Swin-T [15]	87.45	93.31	<b>95.93</b>	68.27	81.14	73.63	86.01	92.48	89.23
	<b>ODFormer (Ours)</b>	<b>88.35</b>	<b>93.82</b>	94.37	<b>74.18</b>	<b>85.18</b>	89.63	<b>88.39</b>	<b>93.83</b>	<b>97.85</b>
DRIONS-DB	FCN [19]	49.28	66.50	68.08	68.48	81.29	70.34	53.77	69.93	53.90
	PSPNet [20]	60.04	75.03	81.13	90.22	94.86	96.05	85.78	92.35	89.98
	FPNNet [22]	32.35	48.89	85.98	87.92	93.57	95.08	84.39	91.53	86.33
	UperNet [16]	30.4	46.63	69.26	89.95	94.71	94.89	78.79	88.14	80.22
	DeepLab v3 [34]	44.93	62.00	81.17	87.01	93.05	96.37	83.76	81.16	87.97
	NonLocal [25]	65.97	79.50	76.92	89.90	94.68	96.90	84.23	91.44	86.94
	ANN [26]	34.62	51.43	83.07	89.82	94.64	96.52	82.26	90.26	87.61
	GCNet [27]	55.09	71.04	89.10	88.57	93.94	98.51	81.53	89.83	86.78
	DANet [28]	57.01	72.62	73.10	89.96	94.71	95.7	82.74	90.55	86.60
	APCNet [35]	40.79	57.94	89.20	82.51	90.42	<b>98.81</b>	74.70	85.52	77.95
	DMNet [29]	45.38	62.43	47.40	72.84	82.28	82.32	41.59	58.75	41.65
	OCRNet [32]	35.86	52.79	<b>91.09</b>	87.13	93.13	97.95	75.06	85.76	79.18
	Swin-T [15]	53.51	69.71	64.23	90.07	94.00	93.91	83.76	91.16	88.27
	<b>ODFormer (Ours)</b>	<b>68.52</b>	<b>81.32</b>	80.22	<b>90.53</b>	<b>95.03</b>	96.64	<b>86.43</b>	<b>92.72</b>	<b>96.80</b>
DRISHTI-GS1	FCN [19]	44.57	61.66	64.08	12.23	21.79	93.74	93.24	96.50	95.72
	PSPNet [20]	63.14	77.41	84.42	63.64	77.78	70.62	92.16	95.92	95.09
	FPNNet [22]	42.68	59.83	91.07	38.26	55.35	99.06	91.21	95.40	96.76
	UperNet [16]	43.73	60.85	87.81	62.75	77.11	70.03	92.12	95.90	96.11
	DeepLab v3 [34]	57.35	72.90	80.07	57.02	72.63	71.29	91.90	95.78	95.25
	NonLocal [25]	58.98	74.30	76.23	41.90	59.05	48.61	91.92	96.32	97.03
	ANN [26]	62.71	76.33	83.64	79.64	45.72	66.72	91.76	95.7	<b>97.18</b>
	GCNet [27]	58.52	73.83	80.30	65.89	79.44	76.94	92.90	96.32	95.36
	DANet [28]	61.48	76.14	79.58	31.86	48.33	<b>99.23</b>	92.91	96.32	97.03
	APCNet [35]	51.85	68.29	67.40	62.78	77.13	66.98	91.93	95.80	96.20
	DMNet [29]	38.06	55.16	38.11	52.80	68.11	74.62	87.91	93.57	91.52
	OCRNet [32]	40.47	57.62	<b>93.07</b>	46.78	63.74	94.03	91.05	95.32	97.09
	Swin-T [15]	40.27	57.41	92.77	83.46	90.29	97.98	92.05	95.86	96.94
	<b>ODFormer (Ours)</b>	<b>63.69</b>	<b>77.81</b>	88.19	<b>83.93</b>	<b>91.27</b>	96.80	<b>93.91</b>	<b>96.86</b>	96.88

of Transformer architectures. Specifically, when compared to Swin Transformer, our ODFormer demonstrates improvements in both Fsc and IoU by approximately 0.51–1.03% and 0.46–1.86%, respectively. Additionally, it can be seen that the Fsc increases by 0.98–20.04%, while the IoU goes up by 0.47–

23.42% when considering the generalizability of the network.

## VI. CONCLUSION

In this article, we conducted a comprehensive study on semantic segmentation, including building a benchmark, de-

veloping a novel network based on Swin Transformer, and proposing a dataset for ONH detection. Experiments verify that our proposed ODFormer can effectively refine the structure of Swin Transformer and thus improve the overall segmentation performance. Additionally, our TongjiU-DCOD dataset, comprising fundus images captured by two distinct cameras, serves to alleviate the scarcity of comprehensive fundus image datasets, thus offering a valuable resource for research and clinical applications. Compared with the SoTA networks, our proposed ODFormer achieves superior performance and produces more robust and accurate results. We believe that the provided benchmark and our proposed dataset are helpful to stimulate further research in this area. Furthermore, our proposed techniques can also be employed to solve other general semantic segmentation problems. In the future, we will continue to explore Transformer-based architectures that can optimize the feature representations effectively and efficiently for ONH detection.

## REFERENCES

- [1] T. Y. Wong, R. Klein, B. E. Klein, J. M. Tielsch, L. Hubbard, and F. J. Nieto, "Retinal microvascular abnormalities and their relationship with hypertension, cardiovascular disease, and mortality," *Survey of ophthalmology*, vol. 46, no. 1, pp. 59–80, 2001.
- [2] C. Sinthanayothin, J. F. Boyce, H. L. Cook, and T. H. Williamson, "Automated localisation of the optic disc, fovea, and retinal blood vessels from digital colour fundus images," *British journal of ophthalmology*, vol. 83, no. 8, pp. 902–910, 1999.
- [3] M. Abdullah, M. M. Fraz, and S. A. Barman, "Localization and segmentation of optic disc in retinal images using circular hough transform and grow-cut algorithm," *PeerJ*, vol. 4, p. e2003, 2016.
- [4] J. Cheng, J. Liu, Y. Xu, F. Yin, D. W. K. Wong, N.-M. Tan, D. Tao, C.-Y. Cheng, T. Aung, and T. Y. Wong, "Superpixel classification based optic disc and optic cup segmentation for glaucoma screening," *IEEE transactions on medical imaging*, vol. 32, no. 6, pp. 1019–1032, 2013.
- [5] K. Rohrschneider, "Determination of the location of the fovea on the fundus," *Investigative ophthalmology & visual science*, vol. 45, no. 9, pp. 3257–3258, 2004.
- [6] L. Zhang and C. P. Lim, "Intelligent optic disc segmentation using improved particle swarm optimization and evolving ensemble models," *Applied Soft Computing*, vol. 92, p. 106328, 2020.
- [7] H. Li and O. Chutatape, "Automatic location of optic disk in retinal images," in *Proceedings 2001 International Conference on Image Processing (Cat. No. 01CH37205)*, vol. 2. IEEE, 2001, pp. 837–840.
- [8] R. Abdel-Ghafar, T. Morris, T. Ritchings, and I. Wood, "Detection and characterisation of the optic disk in glaucoma and diabetic retinopathy," in *Proceedings of medical image understanding and analysis*, 2004, pp. 20–24.
- [9] S. Bharkad, "Automatic segmentation of optic disk in retinal images," *Biomedical Signal Processing and Control*, vol. 31, pp. 483–498, 2017.
- [10] R. Chrastek, M. Wolf, K. Donath, H. Niemann, D. Paulus, T. Hothorn, B. Lausen, R. Lammer, C. Y. Mardin, and G. Michelson, "Automated segmentation of the optic nerve head for diagnosis of glaucoma," *Medical image analysis*, vol. 9, no. 4, pp. 297–314, 2005.
- [11] K. Li, Y. Wang, J. Zhang, P. Gao, G. Song, Y. Liu, H. Li, and Y. Qiao, "Uniformer: Unifying convolution and self-attention for visual recognition," *IEEE Transactions on Pattern Analysis and Machine Intelligence*, 2023.
- [12] R. Fan, K. Alipour, C. Bowd, M. Christopher, N. Brye, J. A. Proudfoot, M. H. Goldbaum, A. Belgith, C. A. Girkin, M. A. Fazio, et al., "Detecting glaucoma from fundus photographs using deep learning without convolutions: transformer for improved generalization," *Ophthalmology science*, vol. 3, no. 1, p. 100233, 2023.
- [13] Y. Feng, Z. Li, D. Yang, H. Hu, H. Guo, and H. Liu, "Polarformer: Optic disc and cup segmentation using a hybrid cnn-transformer and polar transformation," *Applied Sciences*, vol. 13, no. 1, p. 541, 2022.
- [14] R. Hussain and H. Basak, "Ut-net: Combining u-net and transformer for joint optic disc and cup segmentation and glaucoma detection," *arXiv preprint arXiv:2303.04939*, 2023.
- [15] Z. Liu, Y. Lin, Y. Cao, H. Hu, Y. Wei, Z. Zhang, S. Lin, and B. Guo, "Swin transformer: Hierarchical vision transformer using shifted windows," in *Proceedings of the IEEE/CVF international conference on computer vision*, 2021, pp. 10012–10022.
- [16] T. Xiao, Y. Liu, B. Zhou, Y. Jiang, and J. Sun, "Unified perceptual parsing for scene understanding," in *Proceedings of the European conference on computer vision (ECCV)*, 2018, pp. 418–434.
- [17] E. J. Carmona, M. Rincon, J. Garcıa-Feijoo, and J. M. Martın-de-la Casa, "Identification of the optic nerve head with genetic algorithms," *Artificial intelligence in medicine*, vol. 43, no. 3, pp. 243–259, 2008.
- [18] J. Sivaswamy, S. Krishnadas, A. Chakravarty, G. Joshi, A. S. Tabish, et al., "A comprehensive retinal image dataset for the assessment of glaucoma from the optic nerve head analysis," *JSM Biomedical Imaging Data Papers*, vol. 2, no. 1, p. 1004, 2015.
- [19] J. Long, E. Shelhamer, and T. Darrell, "Fully convolutional networks for semantic segmentation," in *Proceedings of the IEEE conference on computer vision and pattern recognition*, 2015, pp. 3431–3440.
- [20] H. Zhao, J. Shi, X. Qi, X. Wang, and J. Jia, "Pyramid scene parsing network," in *Proceedings of the IEEE conference on computer vision and pattern recognition*, 2017, pp. 2881–2890.
- [21] H. Zhou, J. Zhang, J. Lei, S. Li, and D. Tu, "Image semantic segmentation based on fcn-crf model," in *2016 International Conference on Image, Vision and Computing (ICIVC)*. IEEE, 2016, pp. 9–14.
- [22] T.-Y. Lin, P. Dollar, R. Girshick, K. He, B. Hariharan, and S. Belongie, "Feature pyramid networks for object detection," in *Proceedings of the IEEE conference on computer vision and pattern recognition*, 2017, pp. 2117–2125.
- [23] L.-C. Florian and S. H. Adam, "Rethinking atrous convolution for semantic image segmentation," in *Conference on computer vision and pattern recognition (CVPR)*. IEEE/CVF, vol. 6, 2017.
- [24] L.-C. Chen, Y. Zhu, G. Papandreou, F. Schroff, and H. Adam, "Encoder-decoder with atrous separable convolution for semantic image segmentation," in *Proceedings of the European conference on computer vision (ECCV)*, 2018, pp. 801–818.
- [25] X. Wang, R. Girshick, A. Gupta, and K. He, "Non-local neural networks," in *Proceedings of the IEEE conference on computer vision and pattern recognition*, 2018, pp. 7794–7803.
- [26] Z. Zhu, M. Xu, S. Bai, T. Huang, and X. Bai, "Asymmetric non-local neural networks for semantic segmentation," in *Proceedings of the IEEE/CVF international conference on computer vision*, 2019, pp. 593–602.
- [27] Y. Cao, J. Xu, S. Lin, F. Wei, and H. Hu, "Gnet: Non-local networks meet squeeze-excitation networks and beyond," in *Proceedings of the IEEE/CVF international conference on computer vision workshops*, 2019, pp. 0–0.
- [28] J. Fu, J. Liu, H. Tian, Y. Li, Y. Bao, Z. Fang, and H. Lu, "Dual attention network for scene segmentation," in *Proceedings of the IEEE/CVF conference on computer vision and pattern recognition*, 2019, pp. 3146–3154.
- [29] J. He, Z. Deng, and Y. Qiao, "Dynamic multi-scale filters for semantic segmentation," in *Proceedings of the IEEE/CVF International Conference on Computer Vision*, 2019, pp. 3562–3572.
- [30] A. Vaswani, N. Shazeer, N. Parmar, J. Uszkoreit, L. Jones, A. N. Gomez, . Kaiser, and I. Polosukhin, "Attention is all you need," *Advances in neural information processing systems*, vol. 30, 2017.
- [31] R. Strudel, R. Garcia, I. Laptev, and C. Schmid, "Segmenter: Transformer for semantic segmentation," in *Proceedings of the IEEE/CVF international conference on computer vision*, 2021, pp. 7262–7272.
- [32] Y. Yuan, X. Chen, and J. Wang, "Object-contextual representations for semantic segmentation," in *Computer Vision—ECCV 2020: 16th European Conference, Glasgow, UK, August 23–28, 2020, Proceedings, Part VI 16*. Springer, 2020, pp. 173–190.
- [33] A. Dosovitskiy, L. Beyer, A. Kolesnikov, D. Weissenborn, X. Zhai, T. Unterthiner, M. Dehghani, M. Minderer, G. Heigold, S. Gelly, et al., "An image is worth 16x16 words: Transformers for image recognition at scale," *arXiv preprint arXiv:2010.11929*, 2020.
- [34] L.-C. Chen, G. Papandreou, F. Schroff, and H. Adam, "Rethinking atrous convolution for semantic image segmentation," *arXiv preprint arXiv:1706.05587*, 2017.
- [35] J. He, Z. Deng, L. Zhou, Y. Wang, and Y. Qiao, "Adaptive pyramid context network for semantic segmentation," in *Proceedings of the IEEE/CVF Conference on Computer Vision and Pattern Recognition*, 2019, pp. 7519–7528.